JMEPEG (2021) 30:5799–5810
https://doi.org/10.1007/s11665-021-05854-6

1059-9495/$19.00

The Effect of Flood, High-Pressure Cooling, and CO_2-Assisted Cryogenic Machining on Microhardness, Microstructure, and X-ray Diffraction Patterns of NiTi Shape Memory Alloy

O. Kitay and *Y. Kaynak*

Submitted: 2 August 2020 / Revised: 26 March 2021 / Accepted: 18 April 2021 / Published online: 18 May 2021

This study focuses on the effects of various cutting speeds and cutting conditions including dry, CO_2, HPC and flood on the surface integrity characteristics of the machined NiTi alloy. Machining-induced affected layer, microstructure, microhardness and XRD analysis are considered to assess the surface integrity characteristics of NiTi alloy. The findings from this current study reveal that as the cutting speed increased, the depth of the machining-induced layer decreased. While the microhardness value of the machined samples increased in all of the cutting conditions compared to the as-received hardness, the greatest increase was in the CO_2 condition, with 36%. The highest peak intensities of the *B2* main austenite XRD peaks occurred at the cutting speed of 70 m/min. The full width at half maximum values of the XRD peaks increased in all of the cutting conditions, especially at the cutting speed of 20 m/min, and this situation supports the microhardness increase. The smallest crystallite size occurred under the CO_2 condition at the cutting speed of 20 m/min, while the highest dislocation density occurred under the HPC condition at the same cutting speed.

Keywords CO_2, cryogenic machining, crystallite size, high-pressure cooling (HPC), NiTi shape memory alloy, surface integrity, XRD analysis

1. Introduction

Shape memory alloys are widely used in different industries such as aerospace (Ref 1), biomedical (Ref 2), construction (Ref 3), robotic (Ref 4) and fasteners (Ref 5) due to their unique features, such as their shape memory behavior, superelastic property, high strength corrosion and fatigue resistance properties (Ref 6-8). Also, NiTi shape memory alloy shows a solid-state phase transformation from high-temperature austenite phase to low-temperature martensite phase or vice versa (Ref 9). Machining has potential to be more commonly used in producing components made of NiTi alloys. However, shape memory and superelasticity properties of this alloy make machining process difficult (Ref 8, 10).

On the other hand, microstructure of shape memory materials is sensitive to stress and temperature thus in addition to machining process, surface and subsurface of NiTi alloys after machining process requires further attention (Ref 11). In particular, the alterations that occur in the surface integrity characteristics after machining of shape memory alloy materials are an important issue that should be examined in order to determine the final properties and performance of the manufactured components (Ref 12, 13).

While many researchers (Ref 10, 14-17) have already reported that selected cutting parameters in machining NiTi shape memory alloy with different machining methods, such as turning, milling, water jet, and EDM, have a large effect on controlling the surface integrity characteristics such as microstructure, microhardness, phase transformation properties, a few researchers have focused on selected cutting conditions such as cryogenic, flood cooling, minimum quantity lubrication (MQL) and chilled air in terms of the surface integrity characteristics. Traditional machining methods are generally preferred in these studies, since the most applicable machining methods are conventional methods such as turning in examining the effect of the cutting conditions. Kaynak et al. presented the effects of cryogenic machining with liquid nitrogen (LN_2) on the microhardness of the subsurface of the work material and the depth of the machining-induced affected layer (Ref 18). In another study by Kaynak et al. (Ref 19) in the machining operation of room-temperature austenitic NiTi alloy under cryogenic and MQL conditions, the effect of the cutting speed and cutting conditions on phase transformation was examined and XRD analysis showed that a *B19*' martensite peak occurred in the cryogenic condition. Kaynak et al. (Ref 20) investigated the effects of cryogenic machining on the microstructure and reported that the depth of the machining-induced layer was 3 times higher in cryogenic than dry conditions. Weinert et al. (Ref 21) investigated the effects of a hole drilling operation on the hardness and reported an increase of up to 140 μm from the hole edge at low cutting speeds. Kaynak et al. also examined the effect of the machining of NiTi alloy under dry, preheated and cryogenic conditions on the phase transformation temperatures, and also in the XRD analysis it was observed that the *B19*' martensite peaks in the as-received material disappeared

O. Kitay, Department of Machine and Metal Technologies, Bilecik Seyh Edebali University, Bilecik, Turkey; and **Y. Kaynak**, Department of Mechanical Engineering, Marmara University, Goztepe Campus, 34722 Istanbul, Turkey. Contact e-mail: ozhan.kitay@bilecik.edu.tr.

and transformed to *B2* austenite, and in the DSC analysis the phase transformation temperatures changed (Ref 22). Zailania et al. (Ref 23) investigated the effects of chilled air on the microstructure of machined samples. Applying chilled air increased the dendritic structure density and microhardness. In another study, Zailania et al. (Ref 24) showed that using MQL + chilled air together in the micro-milling process creates uniform grain structures.

In the studies on the surface integrity of the NiTi shape memory alloy, it is seen that most of the studies are done on the main features such as microhardness, phase transformation and microstructure. However, studies on the effects of the cutting conditions on the machining-induced shape memory properties and surface integrity characteristics are limited to a few researchers. So, in this study, the surface integrity characteristics of NiTi alloy were investigated in machining operations using high-pressure cooling (HPC) and carbon dioxide (CO_2)-assisted cryogenic cooling conditions. The data obtained from the machining tests were compared with dry and flood conditions considering the previous studies in terms of microstructure, microhardness and XRD analysis.

2. Experimental Setup

The workpiece used in this study was NiTi shape memory alloy [Ni-50.8, Ti-balance (wt.%)] as round bars of 12.5 mm diameter and 80 mm length. The workpiece was produced by the vacuum arc remelting (VAR) method and subjected to hot rolling and full annealing at 750 ºC for 30 minutes. The NiTi alloy was in its austenite phase at room temperature and its microhardness was 295 ± 5 HV. The phase transformation temperatures were determined by differential scanning calorimetry (DSC) where the martensite start (M_s), martensite finish (M_f), austenite start (A_s), and austenite finish (A_f) temperatures are – 32, – 71, – 43, and – 11°C, respectively (Ref 25). A microstructure image of the as-received material is presented in Fig. 1.

The machining experiments were carried out on a Puma GT2100 CNC turning center, which has a maximum spindle speed of 4500 rpm and 18 kW. The cutting tools used in these experiments were Sandvik Coromant DNMG 110404-MF 1105 and the cutting holder was HDJNL 2525M 11HP. Cutting speeds (V_c) were selected as 20, 45 and 70 m/min and the depth of cut (a_p) and feed rate (f) were kept constant at 0.6 and 0.08 mm/rev, respectively.

While dry cutting experiments were performed at room temperature, the flood coolant with a synthetic oil mixture of 5% was applied with a 400 liter/hour flow rate, high-pressure cooling (HPC) was applied with a pressure of 50 bar, and carbon dioxide (CO_2)-assisted cryogenic coolant was applied with 45 bar to the cutting area from the rake face of the cutting tools as a lubricant/coolant. Implementation of the different coolant and lubricants from the rake face is shown in Fig. 2. The cutting temperatures were measured using the Optris PI 400 infrared camera. The emissivity value was taken as 0.21 during the measurements (Ref 26). Cutting forces were measured using the Kistler 2129AA dynamometer.

To examine the microhardness and microstructure, the machined workpieces were cut with diamond cutting disks, following which the cut specimens were cold-mounted in acrylic and polished using 60, 30 and 15 µm grit magnetic disks. The cold-mounted specimens were etched using a solution of 3.2 vol.% HF + 14.6 vol.% HNO_3 + 82.2 vol.% H_2O to review the microstructure (Ref 18). The detail of microstructure examination is presented in Fig. 3. The microstructure of the etched specimens was examined by a Keyence digital optical microscope. The microhardness of the machined workpieces was measured with a Future-Tech FM310e hardness tester. The hardness of each specimen was determined by taking the average of four measurements. For analyzing the phase transformation, x-ray diffraction (XRD) measurements were performed by a Bruker AXS Brand D2 Phaser device with CuKα radiation (λ = 1,54060 A) from the current and voltage values of 10 mA and 30 kv, respectively.

3. Experimental Results

3.1 Cutting Temperature

The high cutting temperature generated between the cutting tool and workpiece during machining is an undesirable condition in terms of machining performance. In fact, the machining performance directly affects the surface integrity characteristics of the machined material. Although increased temperature results in various difficulties and problems including tool wear, causing of surface deterioration in machining various engineering materials, phase state is also included in

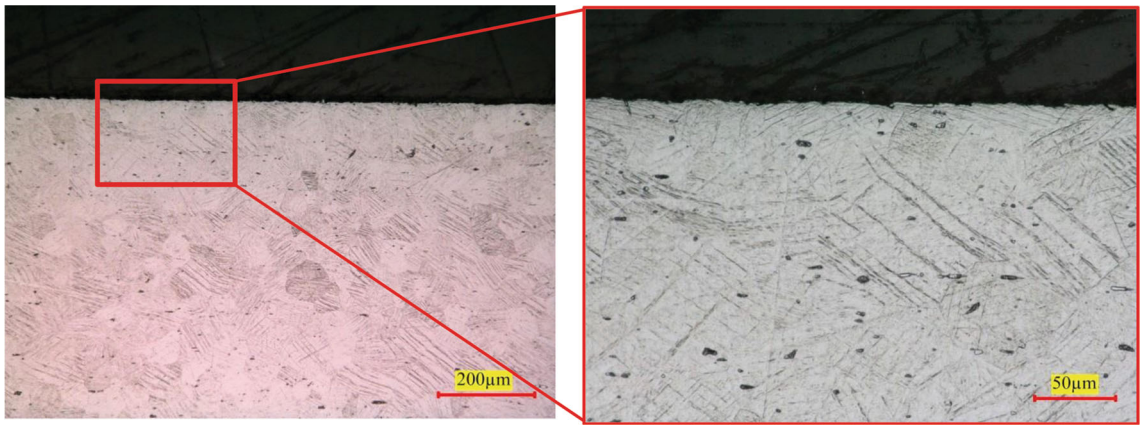

Fig. 1 Microstructure image of as-received NiTi shape memory alloy

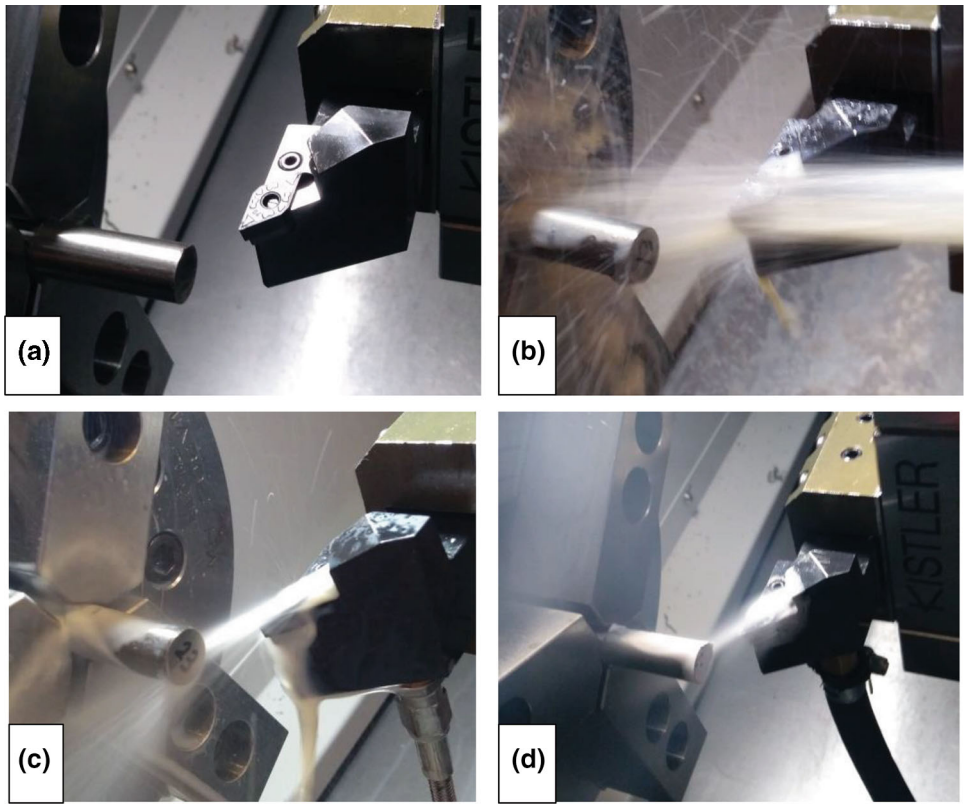

Fig. 2 Applying coolants and lubricants (a) dry (b) flood (c) HPC (d) CO_2

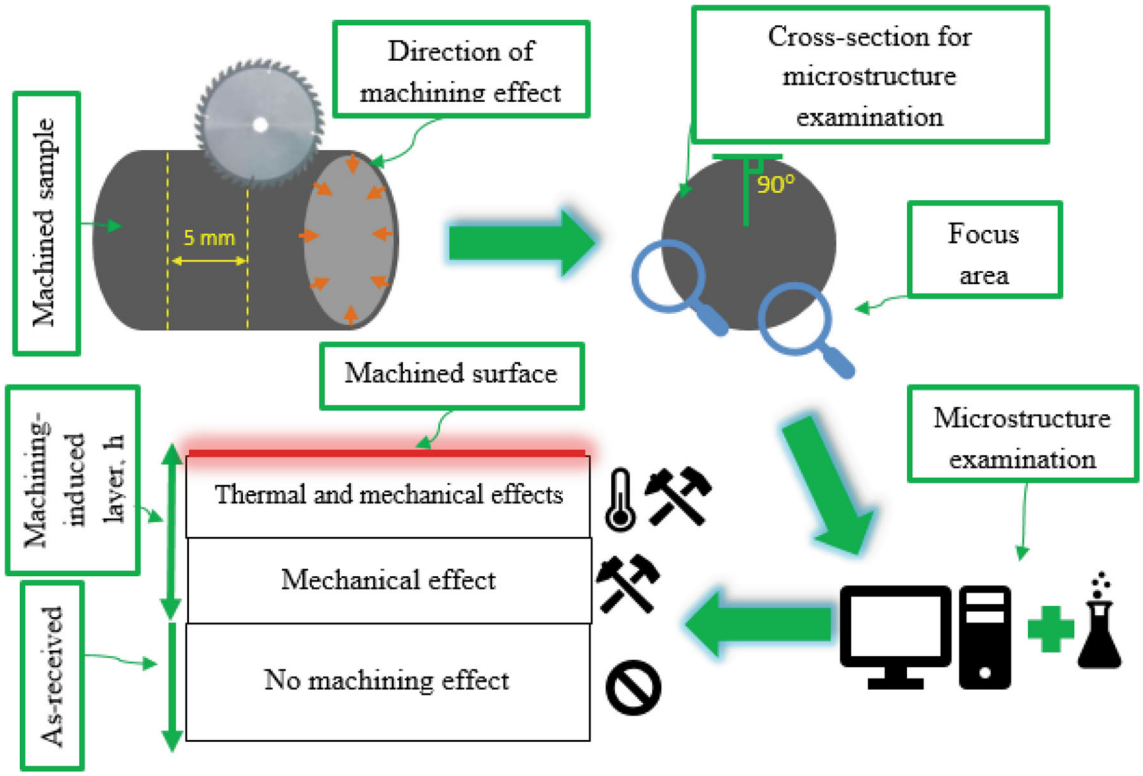

Fig. 3 Microstructure examination steps

shape memory alloys resulting from temperature changes. In this study, the purpose of measuring the cutting temperature is to examine the active phase state of the NiTi alloy during the turning operations.

The measured average cutting temperatures during the machining experiments of NiTi alloy under the dry and CO_2 conditions are presented in Fig. 4 as a function of the cutting speed; it was not possible to make measurements under the HPC and flood conditions with the thermal camera. In general, the temperature in the dry condition is higher than the CO_2 condition, and as the cutting speed increased, the temperature increased in both cutting conditions. The important point here is that even the lowest average cutting temperature is above the austenite temperatures of the material.

Depending on the phase transformation temperature of the NiTi alloy, and cooling condition such as LN_2-assisted cryogenic cooling, phase transformation during cutting process was observed in the literature (Ref 27). But in this current study, it is obvious that even under CO_2-assisted cryogenic cooling condition, the recorded temperature is far from the martensite start temperature. As can be seen in Fig. 4, the average cutting temperatures measured in the CO_2-assisted cryogenic cooling condition were insufficient to transform the active phase of the material. In order for the NiTi alloy to remain in the martensite phase, coolants with more cooling capacity, such as LN_2, are more effective in machining operations (Ref 19). This is mainly because of the boiling point temperature of LN_2 and CO_2 that are – 196°C and – 78°C, respectively, although both gases can be cryogenically applied (Ref 28).

3.2 Cutting Force

It is important to analyze the cutting force as well as the cutting temperature in order to be able to analyze the changes in the surface integrity characteristics. Thus, the results of thermal and mechanical effect occurring in the surface and subsurface regions of the machined NiTi alloy can be better understood. Therefore, the cutting forces measured in the machining experiments performed under different cutting conditions are shown in Fig. 5 as a function of the cutting speed. Overall trend shows that increased cutting speeds results in reduced forces in all cutting conditions. This shows good agreement with the temperature trend presented in the previous section. However, the variation in forces considering 20 and 45 m/min cutting speed is much smaller as compared with 70 m/min cutting speed where the temperature difference is much larger as indicated in Fig. 4. Although notable force variation is observed in dry and flood cooling, in case of CO_2 and HPC no large difference occurs when cutting speed varied. While efficient cooling capability of CO_2 and HPC can be the reason of this result. But overall, these results provide evidence that HPC and CO_2 play effective role on the forces in machining process of NiTi shape memory alloys.

3.3 Microstructure

As NiTi alloys are sensitive to changes in temperature and stress, machining process has potential to affect its surface and subsurface. In fact, considering the Zener–Hollomon equation [29), and the main factors affecting grain refinement occurs in the metallic material are specified as the strain rate and temperature. Eq (1) is

$$Z = \dot{\varepsilon} * exp\left(\frac{Q}{RT}\right) \quad \text{(Eq 1)}$$

where $\dot{\varepsilon}$ is the strain rate, R=8.314 J/kmol is the universal gas constant, T is the absolute temperature (°K) and Q (J/mol) is the activation energy. In this regard, the microstructure of the machined NiTi alloy material has been investigated in terms of temperature and strain on the effect of different lubricants/coolants and variable cutting speeds.

In the machining process, the workpiece is exposed to a number of thermal, mechanical and chemical effects. These effects may cause strain hardening and recrystallization of the material. Therefore, these effects are the main cause of changes in the microstructure of the material, plastic deformation and phase transformations (Ref 30).

The thickness of the machining-induced layers is not the same in the machined samples and depends on the cutting conditions and cutting parameters. So, the microstructure of the machined NiTi alloy should be examined in detail. The microstructure images of machined NiTi alloy under the different cutting conditions are shown in Fig. 6 as a function of the cutting speed. As can be seen in the figure, the machining-induced affected layers (h) on the microstructure

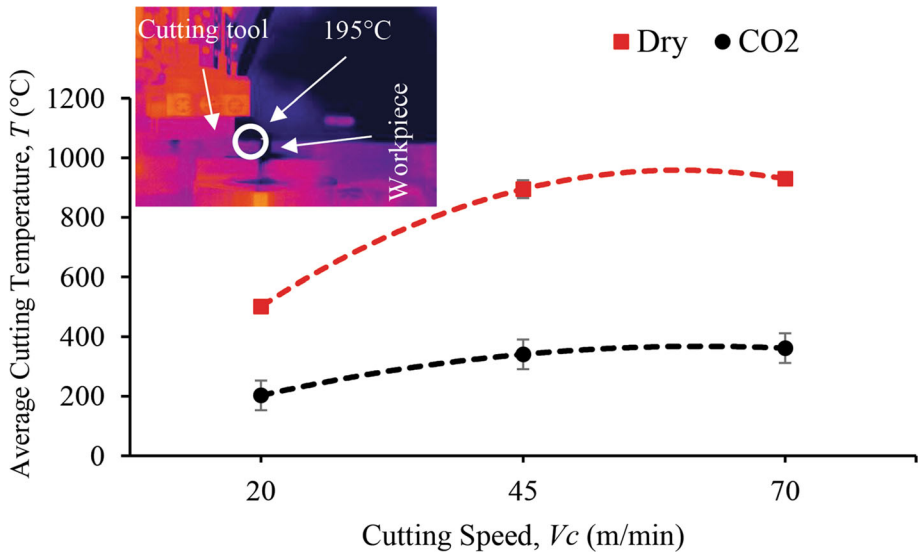

Fig. 4 Average cutting temperature as a function of cutting speed

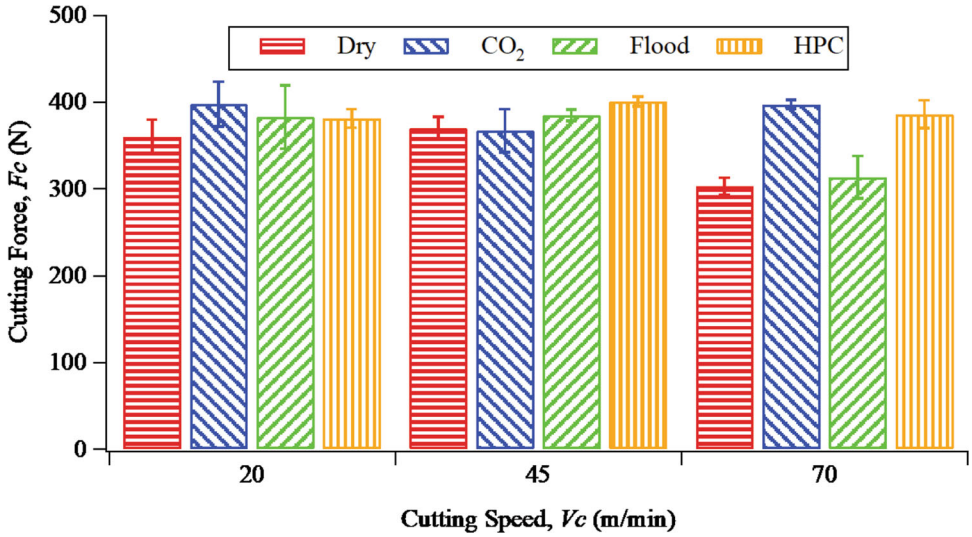

Fig. 5 Measured cutting forces under different cutting conditions as a function of cutting speed

images obtained and the thickness of these layers are not the same. Generally, the density of deformations and twin structures close to the surface region in the pictures can be observed. While the twinning density and orientation are high on the surface regions, the twinning density is lower in the transition layers. When the studies in the literature are considered, it is found that the high density of the twinning structure on the surface and subsurface region causes the grain refinement. Therefore, the plastic deformation is intense in cases where twinned structures are very dense and oriented (Ref 18).

In fact, the twinning-induced deformation and twinning deformation structures that occurred in the NiTi alloy appear to be dislocations that cause plastic deformation because twinning is a plastic deformation mechanism that occurs at low temperatures or high deformation rates. Also, it is well known that the increasing cutting speed increases the cutting temperature. In the light of these explanations, the high cutting temperatures occurring at high cutting speeds during the machining of NiTi alloy resulting an annihilation effect that reduces the plastic deformation. Therefore, the machining-induced affected layer is less at the cutting speed of 70 m/min, especially in the dry condition without coolant and high cutting speeds.

Optical microscopy images show that most of the mentioned twinning structures are dense on the surface and in the subsurface region of the machined samples. In the microstructure images, twinning is intense in some grains, but not with the same density as other grains near them. It is also seen that the twins in the two grains side by side do not have the same angle. In the light of these explanations, the machining-induced affected layers (h) are shown on the microstructures and the measured values are presented in Fig. 7.

The depths of the affected layers presented in Fig. 7 were determined by the average of multiple measurements with the digital optical microscope. At the cutting speed of 20 m/min, the lowest affected layer is dry while the highest is flood and there is a difference of 53%. The average affected layers at the 20 m/min cutting speed were measured as 85 μm in dry, 130 μm in flood, 115 μm in HPC and 100 μm in CO_2 conditions. In fact, as can be seen in the figure, the same ranking trend exists between the cutting conditions at the cutting speed of 70 m/min. Also, in all cutting conditions except CO_2, the affected layer depth tends to decrease with the increasing cutting speed. It is expected that the thickness of the machining-induced layer is high in cryogenic conditions, especially at low cutting speeds. However, the affected layer was less at the cutting speed of 20 m/min. At low cutting speed due to the chip accumulation around the cutting region, the penetration of CO_2 to cutting zone might become difficult and thus this might affect the degree of cold deformation and eventually subsurface response.

3.4 Microhardness

In engineering materials with clear grain boundaries in their microstructure, grain refinement may be observed in the surface areas of the machined material as a result of the machining operation (Ref 31). The hardness increases is expected resulting from the grain refinement. However, after machining process, twinning takes place in the microstructure of NiTi shape memory alloy. The twinning occurrences observed in the surface areas of the machined materials are actually considered as a factor that increases the grain boundaries for NiTi shape memory alloy. Therefore, the increase of the hardness of the machined material can be interpreted by the densities of these twinning formations (Ref 20).

The measured microhardness values of the machined materials under different coolant/lubricant conditions at the 20 m/min cutting speed from the machined surface to the depth of 200 μm are presented in Fig. 8. An increase in the hardness values of the machined material occurred in all the machining operations. The highest average hardness value was 401 HV in the CO_2 condition, and a 36% increase compared to the as-received hardness. In the HPC condition, there was a 29% increase with 382 HV and 18% with 350 HV under the flood condition. In the dry cutting condition, where the hardness value increases the least, there is a 13% increase with 332 HV. The reason for the least increase in the dry cutting condition is that the high cutting temperature due to the lack of coolant or lubricant, as mentioned, leads to annihilation of the plastic deformation.

The changes in the microhardness values of the machined material in the machining operations carried out at the 70 m/

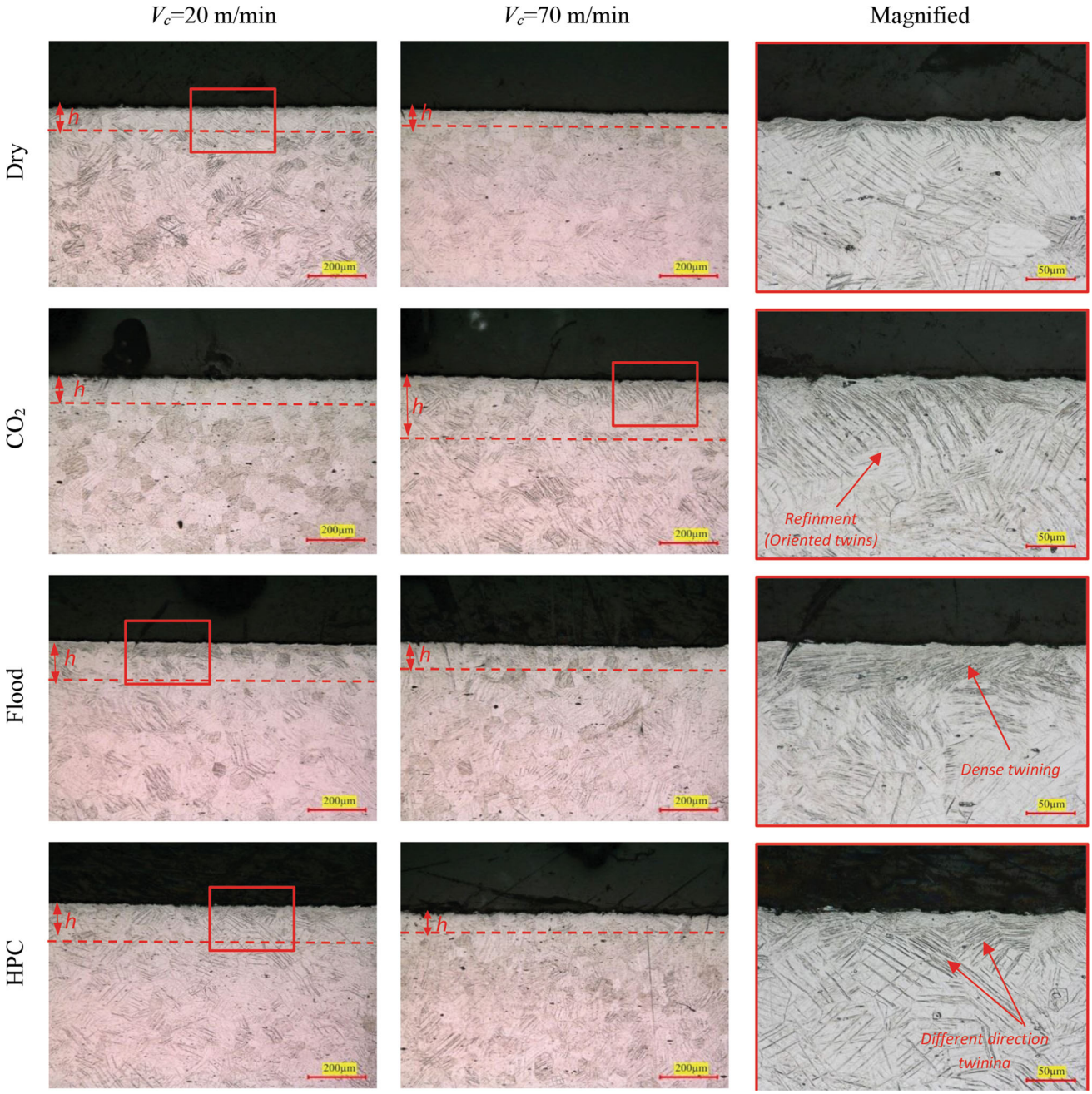

Fig. 6 Microstructure images of machined samples under different cutting conditions

min cutting speed and under different cutting conditions are presented in Fig. 9. As the cutting speed increased from 20 to 70 m/min, there was an increase in the average microhardness values in all cutting conditions, but these hardness values were partially lower. This is due to the thermal softening effect created by the increasing cutting temperature in the cutting area due to the increase of friction between the tool and workpiece with the increase of cutting speed. The highest hardness value was measured as 365 HV under CO_2 conditions and there is a 24% difference compared to the as-received material hardness. The hardness increases occurring in the flood and HPC conditions are almost the same, with a 19 and 17% difference in comparison to the as-received material hardness, with values of 351 and 346 HV, respectively. The least hardness increase was measured under the dry cutting condition with a 334 HV hardness value, and the increase in the hardness value of the material was 13%.

3.5 XRD Phase Analysis

The temperature generated during machining of NiTi shape memory alloys causes the martensite phase of the material to be transformed to austenite and vice versa. Also, one of the reasons that cause the phase transformation of the NiTi alloy is the mechanical stresses that affect the material. Due to the shape memory property of NiTi alloy, phase analysis should be well understood. In this regard, the main peak in the range of 42-43° was examined.

Figure 10 presents the XRD profiles obtained after the machining operation performed at the cutting speed of 20 m/

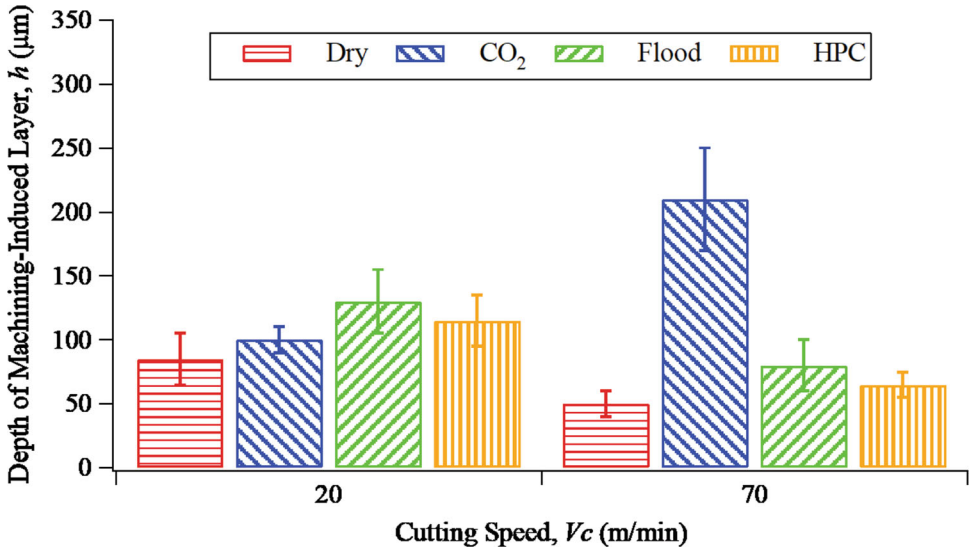

Fig. 7 Average depth of machining-induced layers under different cutting conditions as a function of cutting speed

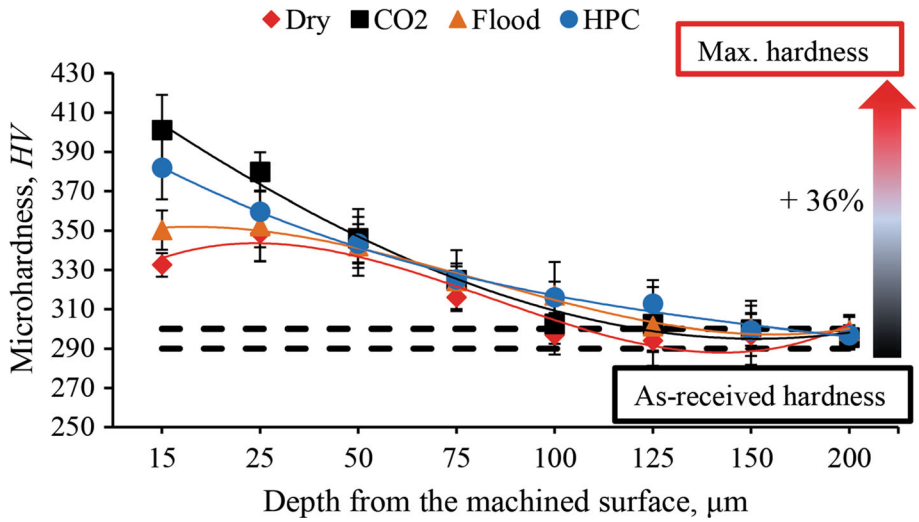

Fig. 8 Microhardness of the machined samples as a function of cutting conditions (V_c=20 m/min)

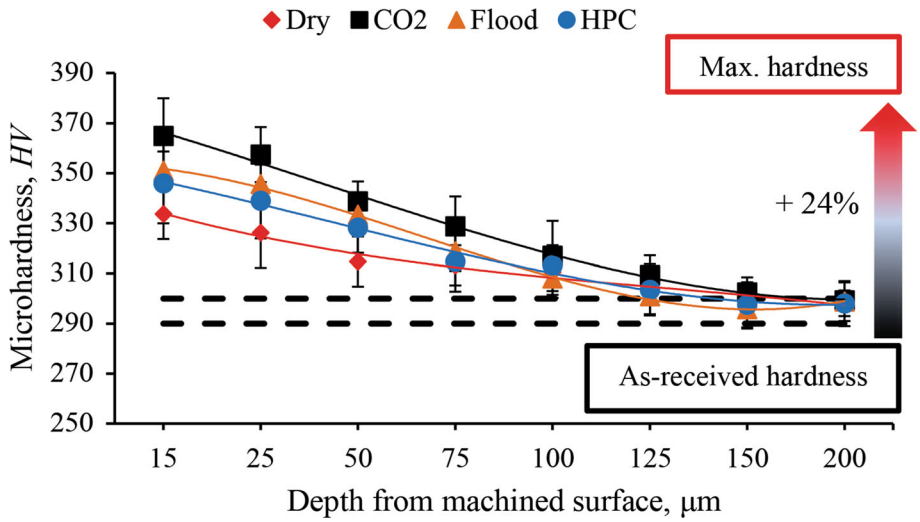

Fig. 9 Microhardness of machined samples as a function cutting conditions (V_c= 70 m/min)

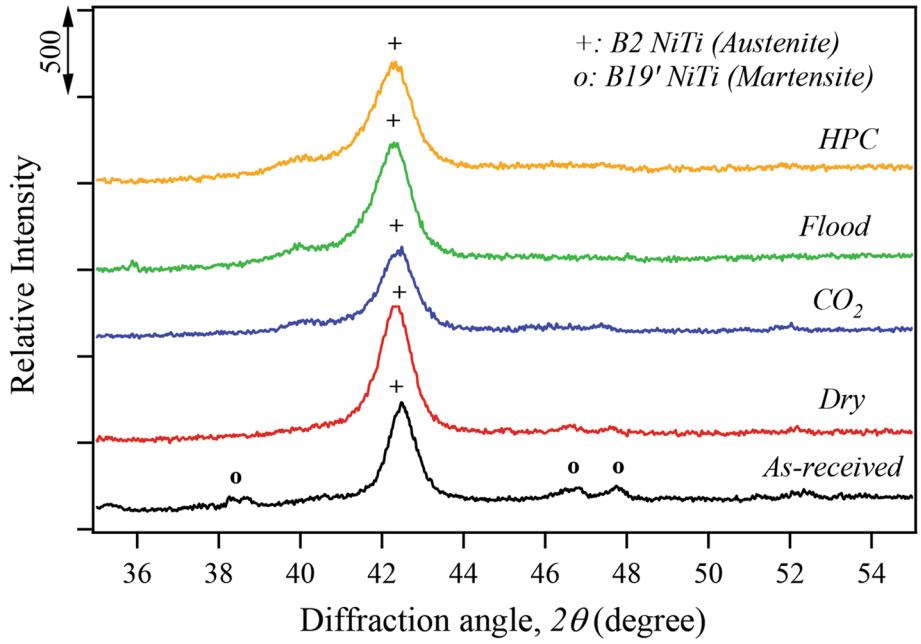

Fig. 10 Comparison of XRD patterns of as-received and samples machined under various conditions at 20 m/min

min and under different cutting conditions. It is seen that there are *B19*' martensite peaks at different diffraction angles in addition to the *B2* main austenite peak in the XRD pattern of the as-received material. It is obvious that after the machining operations, the *B19*' peaks disappeared or rarely survived. In order to determine the proportions of *B2* and *B19'* peaks of the material, the peak intensities as shown in Eqs (2 and 3) can be used:

$$V_{B2} = \frac{I_{B2}}{I_{B2} + I_{B19'}} \quad \text{(Eq 2)}$$

$$V_{B19'} = 1 - I_{B2} \quad \text{(Eq 3)}$$

where V_{B2} is the volume fraction of austenite, $V_{B19'}$ is the volume fraction of martensite, I_{B2} is the peak intensity of the austenite and $I_{B19'}$ is the peak intensity of the martensite [32]). It is also clear that there are shifts in the angles of the peaks of the *B2* of all of the cutting conditions and changes in the peak intensities and widths.

The XRD peak profiles obtained in machining operations carried out at 45 and 70 m/min under different cutting conditions are presented in Fig. 11 and 12, respectively. As can be seen in both graphs, compared to the as-received material, shifts in the peak angles of the machined materials and peak broadenings were obvious. Another important point is that the main peak is fully austenite.

Actually, in order to form peaks of the *B19*' martensite phase, the machining operation must be carried out at very low temperatures considering the transformation temperature. In the machining experiments, it was not possible to go below the martensite start temperature. The measured intensities and shifted angles of the peaks of the XRD profiles are examined in detail in Fig. 13 as a function of the cutting speed. There is a tendency for the peak intensities to increase with the increase in cutting speed. The peak intensities of the machined material at all cutting speeds were measured to be higher than the as-received peak intensity. Here, the CO_2 peak at the 20 m/min cutting speed has exceptional behavior, which can be explained by machining-induced residual stress. Another striking point is that while the dry condition produces the highest peak intensities in general, the CO_2 peak intensity is the highest at the 70 m/min cutting speed. As mentioned earlier, NiTi shape memory alloy is a hard-to-cut material and chip entanglement can occur during machining at high cutting speeds (Ref 14). In such a case, it becomes difficult for the coolant CO_2 to effectively penetrate the cutting area.

Also, there are obvious shifts at all peaks compared to the as-receive peak, which confirms the plastic deformations. The diffraction angle of the main peak of *B2* of the as-received material was 42.478° and all of the machined samples' peak angles are smaller than the as-received material peak angle.

The widths of the peaks were measured to make the XRD analysis more detailed. The full width at half maximum (FWHM) values are given in Fig. 14 to examine the changes in the width of the peaks. As can be seen, the widths of the peaks in all cutting conditions increased compared to the as-received peak. In fact, the peak broadening indicates grain refinement and or dislocation density and hardening in the machined material. As can be seen from the microhardness measurements, the peak broadenings are meaningful. Also, it was stated that twinning in NiTi alloy has an effect on increasing the grain boundary. Considering the Hall–Petch equation shown in Eq (4) (Ref 33), which indicates the relationship between the grain size that can be interpreted as increased grain boundaries and yield strength of the material. This also gives reasonable relation obtained.

$$\sigma_y = \sigma_0 + \frac{k}{\sqrt{D}} \quad \text{(Eq 4)}$$

where σ_y is the yield stress, σ_0 is a frictional stress, k is a constant, D is the grain size.

Considering the crystallite structure of NiTi shape memory alloys that is orthorhombic in the austenite phase and monoclinic in the martensite phase [34]. As x-rays are photon

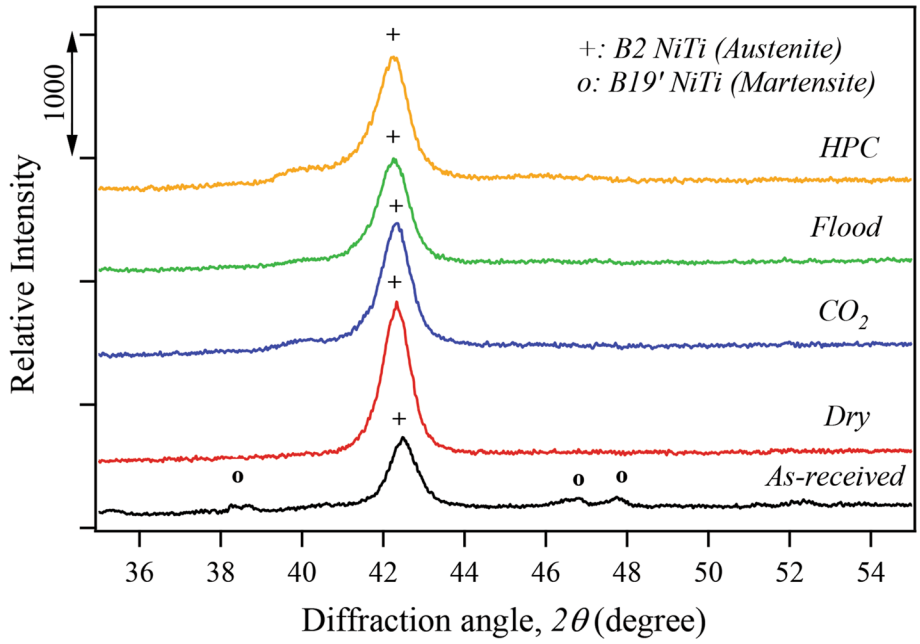

Fig. 11 Comparison of XRD patterns of as-received and samples machined under various conditions at 45 m/min

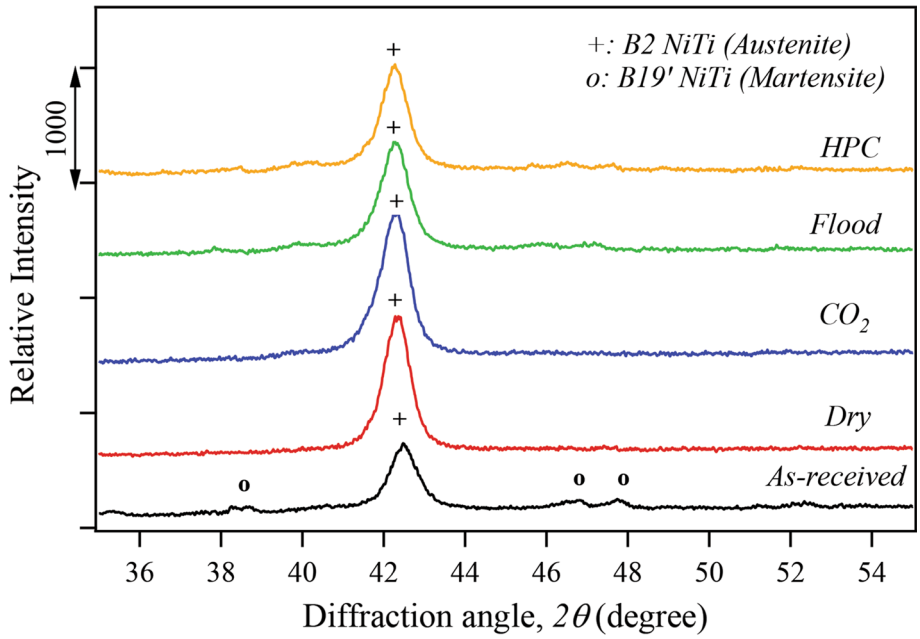

Fig. 12 Comparison of XRD patterns of as-received and samples machined under various conditions at 70 m/min

beams with a wavelength of nanometer dimensions, they can easily penetrate the interior of the material and give information about the crystal structure properties of the material when leaving the material. Thanks to this feature of x-rays, the change in crystallite size caused by machining can be calculated using the Scherrer formula given in Eq (5) as follows:

$$D_c = \frac{K\lambda}{\beta cos\theta} \quad \text{(Eq 5)}$$

where D_c is the crystallite size in nm, K=0.9 is the constant, λ is the wavelength in nm, β is the full width at half maximum (FWHM) in radian, θ is the Bragg diffraction angle in radian (Ref 35). Also, the dislocation density (δ) of the machined material, which is the length of dislocation lines per unit volume (line/m^2), can be calculated with the formula (Ref 36) given in Eq (6) as follows:

$$\delta = \frac{1}{D_C{}^2} \quad \text{(Eq 6)}$$

The changes in the crystallite size and dislocation density of the NiTi alloy after machining are presented in Fig. 15. It is obvious that the crystallite size of all the machined materials has been reduced. This explains the increases in microhardness

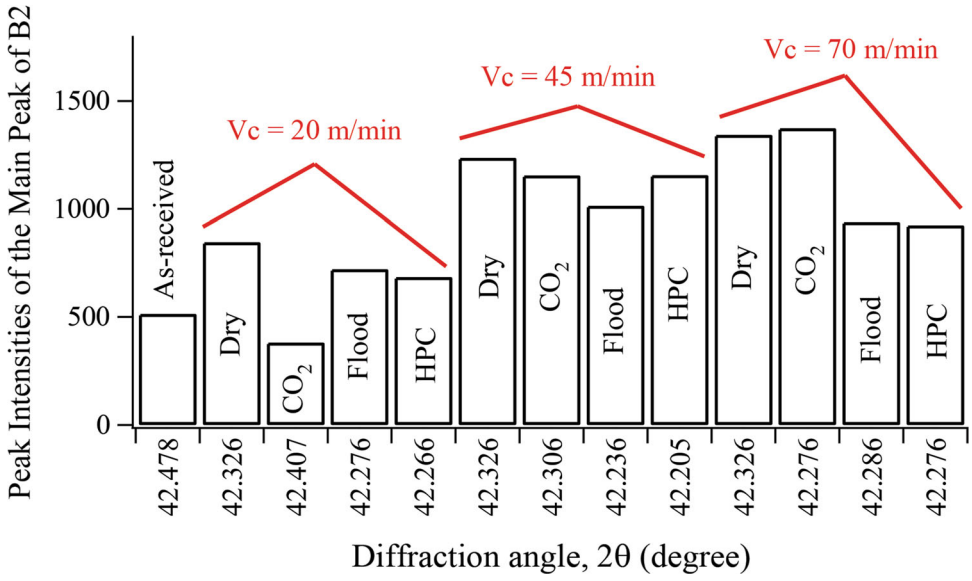

Fig. 13 Comparison of peak intensities and shiftings of the main B2 austenite XRD peaks

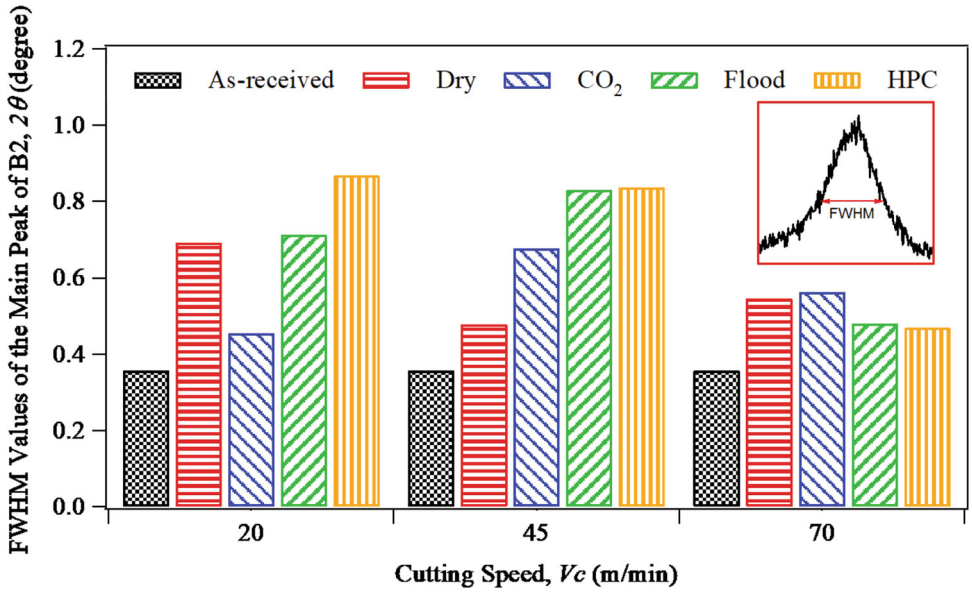

Fig. 14 Comparison of peak broadening at main B2 austenite XRD peaks

and the effect of twinnings on the machined surface and subsurface. In addition, the figure clearly shows that there is a correct proportion between the decrease in crystallite size and the increase in dislocation density.

4. Conclusions

The effect of machining with various cutting speeds and cutting conditions including dry, CO_2, HPC and flood on the surface integrity characteristics of NiTi alloy is demonstrated. The depth of the affected layer decreased in all cutting conditions as the cutting speed increased because of the annihilation effect resulting from the high cutting temperature. On the machined surface and in the subsurface regions, especially at the cutting speed of 20 m/min with lubrication/cooling conditions, the twinning density was higher than the dry condition and the cutting speed of 70 m/min. Increases in the hardness of the machined materials are the result of increased twin density. The highest microhardness values were measured at the cutting speed of 20 m/min under the CO_2 condition as 401 HV. This value is 36% higher than the as-received hardness. Considering the phase transformation temperatures of the NiTi alloy, the effect of the coolant/lubricants used in the machining processes for lowering the cutting temperature could not provide sufficient cooling for the phase transformation. XRD analysis shows that the main peak was *B2* austenite in all cutting conditions. However, the broadening in the XRD peaks is the result of the increases in the hardness of the machined NiTi shape memory alloy. The crystallite sizes of the machined samples were lower than the as-received sample.

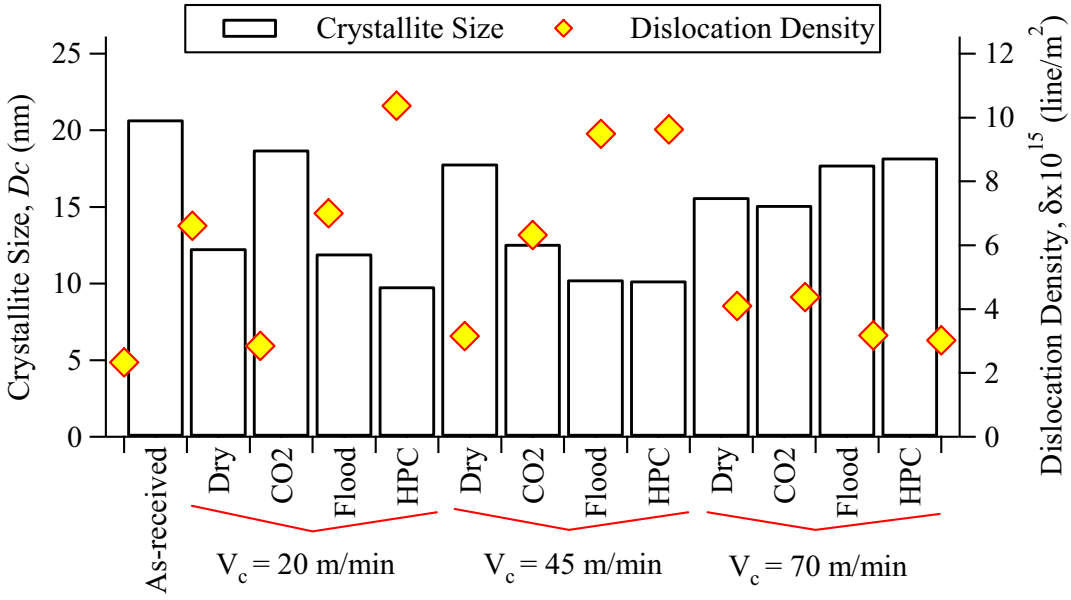

Fig. 15 Crystallite size and dislocation density of the as-received and machined samples

Evidence of such statement is the increased microhardness of machined specimens as compared with as-received one.

Acknowledgment

Financial support from Marmara University Scientific Research Projects Department (BAPKO) under project number FEN-C-YLP-150218-0061 is gratefully acknowledged.

References

1. R. Wanhill and B. Ashok, *Shape Memory Alloys (Smas) for Aerospace Applications Aerospace Materials and Material Technologies*, Springer, 2017, p 467–481
2. L. Machado and M. Savi, Medical Applications of Shape Memory Alloys, *Braz. J. Med. Biol. Res.*, 2003, **36**(6), p 683–691
3. M. Dolce and D. Cardone, Mechanical Behaviour of Shape Memory Alloys for Seismic Applications 1 Martensite and Austenite NiTi Bars Subjected to Torsion, *Int. J. Mech. Sci.*, 2001, **43**(11), p 2631–2656
4. Q. Chang-Jun, M. Pei-Sun and Y. Qin, A Prototype Micro-Wheeled-Robot using SMA Actuator, *Sens. Actuators, A*, 2004, **113**(1), p 94–99
5. T. Duerig and K. Melton, Applications of Shape Memory in the USA, *New Mater. Process. Future*, 1989, **29**, p 195–200
6. D.C. Lagoudas, *Shape Memory Alloys: Modeling and Engineering Applications*, Springer, Boston, 2008
7. S.A. Shabalovskaya, On The Nature of the Biocompatibility and on Medical Applications of NiTi Shape Memory and Superelastic Alloys, *Bio-Med. Mater. Eng.*, 1996, **6**(4), p 267–289
8. L. Selvarajan, R. Rajavel, B. Prakash, D.G. Mohan and S. Gopi, Investigation on Spark Electrical Discharge Machining of Si3N4 Based Advanced Conductive Ceramic Composites, *Mater. Today: Proc.*, 2020, **27**, p 2174–2178
9. K. Bhattacharya, *Microstructure of Martensite: Why It Forms and How It Gives Rise to the Shape-Memory Effect*, Vol 2 Oxford University Press, 2003
10. M. Kong, D. Axinte and W. Voice, Challenges in Using Waterjet Machining of NiTi Shape Memory Alloys: An Analysis of Controlled-Depth Milling, *J. Mater. Process. Technol.*, 2011, **211**(6), p 959–971
11. Field, M., K. JF, and C. JT, A Review of Measuring Methods for Surface Integrity. 1972
12. Y. Kaynak, T. Lu and I. Jawahir, Cryogenic Machining-Induced Surface Integrity: A Review and Comparison with Dry, MQL, and Flood-Cooled Machining, *Mach. Sci. Technol.*, 2014, **18**(2), p 149–198
13. B. Griffiths, *Manufacturing Surface Technology: Surface Integrity and Functional Performance*, Elsevier, 2001
14. K. Weinert and V. Petzoldt, Machining of NiTi Based Shape Memory Alloys, *Mater. Sci. Eng., A*, 2004, **378**(1–2), p 180–184
15. Y. Guo, A. Klink, C. Fu and J. Snyder, Machinability and Surface Integrity of Nitinol Shape Memory Alloy, *CIRP Ann.*, 2013, **62**(1), p 83–86
16. G. Wang, Z. Liu, J. Niu, W. Huang and Q. Xu, Work Hardening Influencing ON Shape Memory Effect of NiTi Alloy by Varying Milling Speeds, *Smart Mater. Struct.*, 2019, **28**(10), p 105034
17. Gaikwad, M.U., A. Krishnamoorthy, and V.S. Jatti, Investigation on effect of process parameter on surface integrity during electrical discharge machining of NiTi 60. *Multidiscipline Modeling in Materials and Structures*, 2020
18. Y. Kaynak, H. Karaca and I. Jawahir, Cutting Speed Dependent Microstructure and Transformation Behavior of NiTi alloy in Dry and Cryogenic Machining, *J. Mater. Eng. Perform.*, 2015, **24**(1), p 452–460
19. Y. Kaynak, Machining and Phase Transformation Response OF Room-Temperature Austenitic NiTi Shape Memory Alloy, *J. Mater. Eng. Perform.*, 2014, **23**(9), p 3354–3360
20. Y. Kaynak, H. Tobe, R. Noebe, H. Karaca and I. Jawahir, The Effects Of Machining on the Microstructure and Transformation Behavior of NiTi Alloy, *Scripta Mater.*, 2014, **74**, p 60–63
21. K. Weinert, V. Petzoldt and D. Kötter, Turning and Drilling of NiTi Shape Memory Alloys, *CIRP Ann.*, 2004, **53**(1), p 65–68
22. Y. Kaynak, B. Huang, H. Karaca and I. Jawahir, Surface Characteristics of Machined NiTi Shape Memory Alloy: The Effects of Cryogenic Cooling and Preheating Conditions, *J. Mater. Eng. Perform.*, 2017, **26**(7), p 3597–3606
23. Z.A. Zailani and P.T. Mativenga, Effects of Chilled Air on Machinability of NiTi Shape Memory Alloy, *Procedia Cirp*, 2016, **45**, p 207–210
24. Z.Z. Abidin, P.T. Mativenga and G. Harrison, Chilled Air System and Size Effect in Micro-Milling of Nickel– Titanium Shape Memory Alloys, *Int. J. Precis. Eng. Manuf.-Green Technol.*, 2020, **7**(2), p 283–297
25. Y. Kaynak, S. Robertson, H. Karaca and I. Jawahir, Progressive Tool-Wear in Machining of Room-Temperature Austenitic NiTi Alloys: The Influence of Cooling/LUBRICATING, Melting, and Heat Treatment Conditions, *J. Mater. Process. Technol.*, 2015, **215**, p 95–104

26. Y. Kaynak, H. Karaca, R. Noebe and I. Jawahir, Tool-Wear Analysis In Cryogenic Machining of NiTi Shape Memory Alloys: A Comparison Of tool-Wear Performance with Dry and MQL Machining, *Wear*, 2013, **306**(1–2), p 51–63
27. Y. Kaynak, H.E. Karaca, R.D. Noebe and I. Jawahir, The Effect of Active Phase of the Work Material on Machining Performance of a NiTi Shape Memory Alloy, *Metall. and Mater. Trans. A.*, 2015, **46**(6), p 2625–2636
28. F. Pusavec, A. Deshpande, S. Yang, R. M'Saoubi, J. Kopac, O.W. Dillon Jr. and I. Jawahir, Sustainable Machining of High Temperature Nickel Alloy–Inconel 718: part 1–Predictive Performance Models, *J. Clean. Prod.*, 2014, **81**, p 255–269
29. C. Zener and J.H. Hollomon, Effect of Strain Rate Upon Plastic Flow of Steel, *J. Appl. Phys.*, 1944, **15**(1), p 22–32
30. D. Ulutan and T. Ozel, Machining Induced Surface Integrity in Titanium and Nickel Alloys: A Review, *Int. J. Mach. Tools Manuf*, 2011, **51**(3), p 250–280
31. Z. Pu, J. Outeiro, A. Batista, O. Dillon Jr., D. Puleo and I. Jawahir, Enhanced Surface Integrity of AZ31B Mg Alloy by Cryogenic Machining Towards Improved Functional PERFORMANCE of Machined Components, *Int. J. Mach. Tools Manuf*, 2012, **56**, p 17–27
32. R. Pederson, O. Babushkin, F. Skystedt and R. Warren, Use of High Temperature X-ray Diffractometry to Study Phase Transitions and Thermal Expansion Properties in Ti-6Al-4V, *Mater. Sci. Technol.*, 2003, **19**(11), p 1533–1538
33. M.A. Meyers and K.K. Chawla, *Mechanical Behavior of Materials*, Cambridge University Press, 2008
34. C. Velmurugan, V. Senthilkumar, S. Dinesh and D. Arulkirubakaran, Machining of NiTi-Shape Memory Alloys-A Review, *Mach. Sci. Technol.*, 2018, **22**(3), p 355–401
35. A. Monshi, M.R. Foroughi and M.R. Monshi, Modified Scherrer Equation to Estimate More Accurately Nano-Crystallite Size Using XRD, *World J Nano Sci Eng*, 2012, **2**(3), p 154–160
36. G. Williamson and R. Smallman III., Dislocation Densities in Some Annealed and Cold-Worked Metals from Measurements on the X-ray Debye-Scherrer Spectrum, *Phil. Mag.*, 1956, **1**(1), p 34–46